CRYSTAL GROWTH & DESIGN

Article

pubs.acs.org/crystal

Reversible Solid-State Transformation in $\{Ni_2(H_2O)_2(Bpa)_2\}(V_6O_{17})$ Proved by Synchrotron Radiation: Color and Magnetic Properties Change

Roberto Fernández de Luis, Joseba Orive, Edurne S. Larrea, M. Karmele Urtiaga, and María I. Arriortua*

Departamento de Mineralogía y Petrología, Facultad de Ciencia y Tecnología. Universidad del País Vasco, UPV/EHU. Apdo. 644, E-48080 Bilbao, Spain

Supporting Information

ABSTRACT: The 3D crystal structure of $\{Ni_2(H_2O)_2(Bpa)_2\}(V_6O_{17})$ (NiBpaRT), were Bpa is 1,2-bis(4-pyridil)ethane, was determined by single crystal X-ray diffraction. The crystal structure is constructed from $\{Ni(H_2O)(Bpa)\}$ metal−organic and $(V_3O_{8.5})$ vanadate chains. The connectivity of these one-dimensional units generates a three-dimensional inorganic substructure, and also a three-dimensional inorganic−organic framework. The asymmetric unit contains two crystallographically pseudoequivalent vanadate and metal−organic chains. The stacking of these crystallographically pseudoequivalent units seems to be nearly related to the twinning law of the crystals, and with the diffuse scattering observed in the diffraction pictures. Several models of local disorders for the packing of these one-dimensional units have been proposed to explain the origin of the diffuse scattering observed in the diffraction images. The obtained single crystals are systematically twinned. The origin of this twining is clearly related to the packing of the crystallographically independent chains along the [100] direction. The topology of the crystal structure is a new self-catenated three nodal net. The simplified structure can be described also as the natural tiling of two different tiles. NiBpaRT shows a reversible solid state transformation due to the loss of coordinated water molecules at 180 °C. The high temperature compound, $\{Ni_2(Bpa)_2\}(V_6O_{17})$ (NiBpaHT), maintains the crystallinity, but the solid state transformation involves a single crystal to polycrystalline reaction. So, the determination of the high temperature structure have been carried out by rigid body Rietveld refinement of the room temperature crystal structure, from synchrotron X-ray diffraction radiation. The loss of coordinated water molecules of the nickel cations is compensated by the incorporation of the terminal oxygen atoms, belonging to the adjacent VO_4 tetrahedra, into the coordination environment of the nickel cations. We have referred to this mechanism of reorganization of the structural units as padlock solid state transformation. The UV−vis spectra corroborate the presence of octahedrally coordinated nickel cations in the high temperature crystal structure. The IR and Raman spectra show strong changes in the absorption maxima related to the stretching vibration of V═O terminal bonds, in good agreement with the proposed padlock mechanism. The dimeric ferromagnetic coupling of the nickel cations through the VO_4 tetrahedra is similar for NiBpaRT and NiBpaHT, showing also an antiferromagnetic coupling at low temperatures. However, the distortion of the nickel coordination environment during the transformation implies an important difference in the *g* values for NiBpaRT and NiBpaHT.

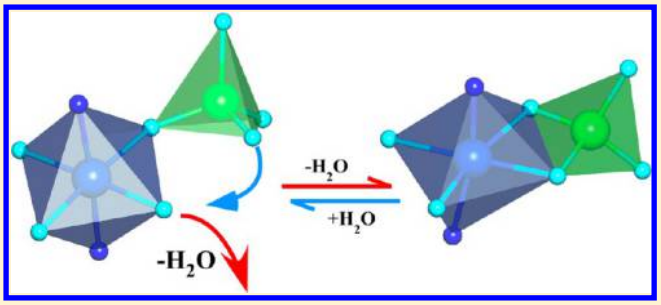

INTRODUCTION

Many interesting solid-state transformations of coordination polymers driven by thermal treatments, photochemical reactivity, or guest replacements have been reported.[1] The reaction mechanisms in solid state transformations involve the generation and cleavage of new covalent bonds. Concretely, for the reactions driven by the removal/uptake of coordinated solvents two general mechanisms have been described: (i) the structural transformations take place due to the bonding of the unused donor atoms of the already attached ligand to the metal center[2] or (ii) the vacant coordination site is fulfilled by the free donor site of another ligand or solvent molecule.[3] Those structural transformations could give rise to a dimensionality increase or decrease of the crystal framework.[4] However, solid state reactions in inorganic compounds or within the inorganic skeleton of inorganic−organic compounds are still quite rare, because they involve movements, and the consequent rearrangement, of less mobile inorganic polyhedra.[5] The reversibility of these solid state reactions is hindered because of the strong character of the generated metal−oxygen bonds. Usually, the structural transformations within the inorganic skeleton imply a hard loss of crystallinity,[6] or in the better cases the loss of their single crystal nature, hindering the study of the molecular movements after the solid state reaction.

The synthesis of inorganic−organic compounds combining flexible inorganic and metal−organic substructures is a very

Received: October 17, 2013
Revised: December 19, 2013
Published: January 3, 2014

Scheme 1

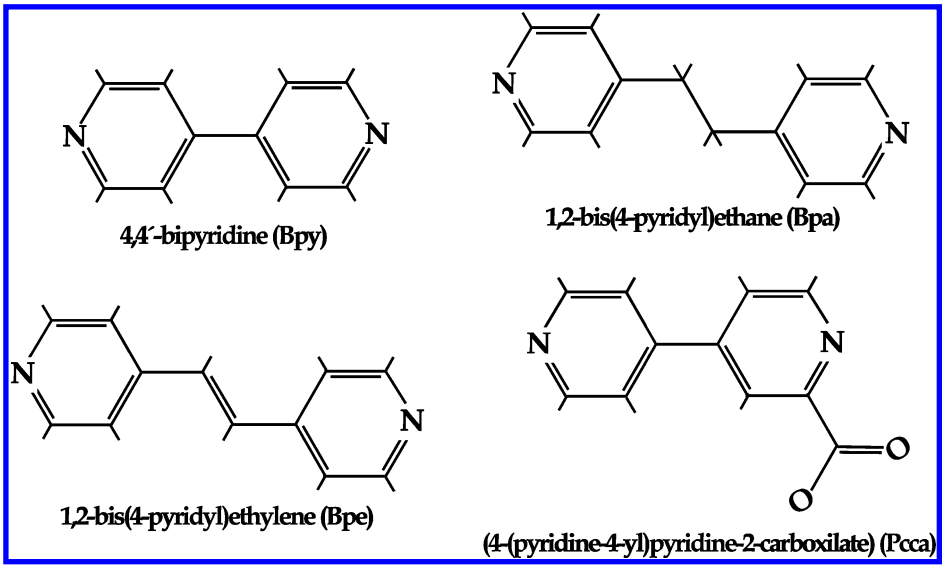

interesting strategy to obtain reversible structural transformations within the inorganic framework of the crystal structures. In that regard, the rich crystal chemistry of the hybrid vanadates allows to combine the great diversity and connectivity of the vanadium oxide subunits with the metal−organic scaffolds generated by the metal−ligand connectivity.[7] Previously reported architectures show the synergetic intergrowing of three-dimensional inorganic and metal−organic sublattices in the same crystal structure. As far as we know, this type of crystal architecture has not been observed in MOFs.[8] Moreover, the variability of the vanadium oxide subunits according to the initial synthesis conditions (pH, concentration, initial stoichiometry, temperature...) increases the diversity of the structures by the combination of the same initial reagents. The thermal stability and thermal response of hybrid vanadates to the loss of guest or coordinated molecules is closely related to the crystal framework itself, and more specifically with the combination of rigid or flexible inorganic and metal−organic subnets within the crystal structure. For example, the rigid three-dimensional inorganic scaffolds stabilized by rigid organic pillars in $[\{Ni_6(H_2O)_{10}(Bpy)_6\}V_{18}O_{51}]\cdot 1.5H_2O$ and $[\{Ni(H_2O)_2(Bpe)\}V_4O_{11}]\cdot 0.5H_2O$, where Bpy is 4,4′-bipyridil and Bpe is 1,2-bis(4-pyridil)ethylene, give rise to irreversible loss of coordinated water molecules with drastic reduction of the crystallinity during the heating process and practically no changes associated with the removal of crystallization water molecules.[9] The crystal structures of $[\{Mn(Bpy)\}(VO_3)_2]\cdot(H_2O)_{1.16}$ and $[\{Mn(Bpy)_{0.5}\}(VO_3)_2]\cdot(H_2O)_{0.62}$ exhibit dynamic and reversible responses to the loss/uptake of crystallization water molecules.[10] Intermediate behaviors are observed in $[\{Ni_8(Bpy)_{16}\}V_{24}O_{68}]\cdot 8.5(H_2O)$ and $[\{Ni_3(H_2O)_3(Bpa)_4\}(V_6O_{18})]\cdot 8H_2O$, because of the combination of both three-dimensional metal−organic and inorganic scaffolds in the same crystal architectures.[11] An interesting example is the $[\{M_2(H_2O)_2(Bpe)_2\}(V_4O_{12})]\cdot 4H_2O\cdot Bpe$ (M = Ni, Co) hybrid vanadate family, which exhibits reversible removal and uptake of coordinated water molecules with a drastic loss of crystallinity associated to the process. The dynamic and reversible single crystal to single crystal transformation because of the removal/addition of coordinated water molecules in $[Co_2(ppca)_2(H_2O)(V_4O_{12})_{0.5}]$ (ppca = 4-(pyridine-4-yl)pyridine-2carboxilate) generates changes in the coordination environment of the Co(II) metal centers, and hence to an appreciable change in the sample color.[12] The variation of the coordination environment of the metal centers gives rise to interesting changes in the physical properties such as color, leading to materials with potential applications in sensing devices. Moreover, the existence of coordinated unsaturated metal sites is very beneficial in porous materials, providing Lewis acid sites in the structure, usable for the surface postfunctionalization for specific catalytic reactions.[13]

Herein, we report the padlock reversible solid state transformation from $\{Ni_2(H_2O)_2(Bpa)_2\}(V_6O_{17})$ (NiBpaRT) to $\{Ni_2(Bpa)_2\}(V_6O_{17})$ (NiBpaHT), (Bpa =1,2-bis(4-pyridil)-ethane). This is an amazing example of how the nonbonded donor atoms of the inorganic polyhedra could complete the coordination environment of the metal centers after the loss of coordinated water molecules. The crystal structures are analyzed, and the topology determined for both compounds. The infrared and Raman spectra of the room temperature and high temperature compounds are discussed, and the change in the magnetic properties explained. Moreover, the possible origin for the diffuse scattering observed in the diffraction images is proposed, and the relationship between the crystal structure and the systematic twinning of the single crystals explained.

EXPERIMENTAL SECTION

Materials and Methods. Commercially available reagent grade chemicals were purchased from Sigma-Aldrich. These were used without further purification. All synthetic reactions were carried out in 50 mL Parr Teflon-lined acid digestion bombs.

Synthesis of NiBpaA. A mixture consisting of $NaVO_3$ (1.04 mmol), 1,2-Di(4-pyridyl)ethane (Bpa) (0.13 mmol), $Ni(NO_3)_2\cdot 6H_2O$ (0.26 mmol), and H_2O (30 mL) in the molar ratio 6:1:2 was placed in a 50-mL Parr Teflon-lined autoclave. The initial pH value was adjusted to 6.0 with 1 M HNO_3 solution under vigorous stirring. The autoclave was sealed and heated for 3 days at 120 °C. After the reaction, strongly twinned yellow single crystals of NiBpaRT were obtained. The chemical composition was calculated from atomic absorption spectroscopy (AES) and C, N, H elemental analysis. Calcd. for $\{Ni_2(H_2O)_2(Bpa)_2\}(V_6O_{17})$: H 2.57%, C 26.22%, N 5.10%, V 27.80%, Ni 10.68%. Found: H 3.20(4)%, C 26.08(3)%, N 5.15(4)%, V 27.75(2)%, Ni 10.98(2)%.

dx.doi.org/10.1021/cg401540s | Cryst. Growth Des. 2014, 14, 658−670

The samples were characterized by powder X-ray diffraction. The patterns were recorded on a Bruker Advance Vário diffractometer ($CuK\alpha_1$ radiation) (2θ range = 5−70°, step size = 0.015°, exposure time = 10 s per step). The Rietveld refinement with a fixed structural model, confirms the inexistence of impurities, despite problems in the fit of some reflections intensity due to the preferred orientation of the samples. The density was measured by the flotation method in a mixture of bromoform/chloroform being 2.00(1) g cm^{-3}.

Single-Crystal X-ray Diffraction: NiBpaRT Crystal Structure Determination. For NiBpaRT, the single-crystal X-ray diffraction data were acquired at 293 K on an Oxford Diffraction XCalibur2 diffractometer with a CCD detector and graphite-monocromated Mo$K\alpha$ radiation. Details of crystal data and some features of the structure refinements are reported in Table 1. Lattice constants were

Table 1. Crystal Data and Structure Refinement for NiBpaRT

compound	NiBpaRT
formula	$C_{24}H_{28}N_4Ni_2O_{19}V_6$
fw (g/mol)	1099.53
cryst syst	monoclinic, P
color	yellow
space group, no.	$P2/c$, 13
a (Å), b (Å), c (Å)	19.6177(10), 9.3725(3), 26.6897(17)
β (deg)	132.445(8)
Z, F(000), T(K)	4, 2172, 293
μ (mm^{-1})	2.562
cryst size (mm)	0.23 × 0.15 × 0.14
radiation (λ(Å))	0.71073
no. of reflns	8448
reflns ($I > 2\sigma(I)$)	7852
h, k, l intervals	$-26 \geq h \geq 26$, $-12 \geq k \geq 12$, $-34 \geq l \geq 34$
R(int), $R(\sigma)$	0.0530, 0.0362
R1, wR2(obs)[a] ($I > 2\sigma(I)$)	0.0925, 0.2241
R1, wR2(all)[a]	0.0979, 0.2315
GOF	1.06
no. params/restraints	450, 0
largest diff. peak (e $Å^{-3}$)	6.244
largest diff. hole (e $Å^{-3}$)	−1.197

[a] $R1 = (\sum w||F_0| - |F_c||)/(\sum w|F_0|)$; $wR2 = ((\sum w((F_0)^2 - (F_c)^2)^2)/((\sum w((F_0)^2)^2)^{1/2}$; $GOF = ((\sum w((F_0)^2 - (F_c)^2)^2)/((n-p))^{1/2}$.

obtained by using a standard program belonging to the diffractometer software, confirming at the same time the good quality of the single-crystal. The Lorentz polarization and absorption corrections were made with the diffractometer software, taking into account the size and shape of the crystal.[14] The structure was solved by direct methods (SIR-92).[15] The refinement of the crystal structure was performed by full-matrix least-squares based on F^2, using the SHELX97 program.[16]

The crystal of NiBpaRT is a pseudomerohedral twin. Both components of the twin are related by the twin law: (1 0 1, 0 −1 0, 0 0 −1). The visual analysis of the diffraction images show strongly overlapped diffraction spots at high angles. Even at low angles, the existence of two components is observed. To solve the twinning, the cells of both components were indexed and the twin law obtained. The reduction was carried out, and the data were treated, taking into account different overlap limits for the diffraction maxima of both components of the twin. The crystal structure was refined with the hkl file containing the intensity data of both components of the twin. Despite the final model was correctly solved, nonpositive anisotropic thermal displacements were obtained for all the atoms during the refinement. In that point of the study, and taking into account that most of the diffraction maxima of both components of the twin were strongly or completely overlapped, the reduction of the data was done integrating both components of the twin with the same cell. R(int) and $R(\sigma)$ values of the data were substantially lowered. The two component twin law was introduced in the crystal structure refinement, giving rise to an important improvement of the R values, and in the anisotropic thermal displacement of the atoms. After the refinement, the masses of both components of the twin were found to have percentages of 59.7(2)% and 40.3(2) %. The crystal structure of NiBpaRT was solved in the monoclinic $P2/c$ space group, which allowed obtaining the positions of vanadium, nickel, and oxygen atoms. Carbon atoms were located in the difference density map. Anisotropic thermal parameters were used for all atoms except for the hydrogen atoms belonging to the organic ligand, which were fixed geometrically and allowed to ride on their parent atoms (C−H = 0.95 Å, U_{iso}(H)= 1.2U_{eq}(C) $Å^2$). The pyridyl rings of the organic ligand were fitted to a regular hexagon (d = 1.39 Å). The hydrogen atoms belonging to the coordinated water molecules (O(1) and O(12) were not located. After the refinement, the most intense residual density maxima are of approximately ±6 e^- $Å^3$, however they are located at 1 Å of the nickel metal centers. The reasons for these suspicious density maxima are the existence of the twinnig and the presence of strong diffuse scattering in the (h0l), (h1l), (h2l), (h3l), ... planes. A qualitative explanation for the strong diffuse scattering is discussed in the Crystal Structure section.

Powder X-ray Diffraction Refinement of the Crystal Structure of NiBpaHT. The NiBpaRT to NiBpaHT solid state transformation gives rise to the destruction of the single crystals, but the crystallinity is maintained after the removal of the coordination water molecules. The powder patterns of the sample at 180 °C were collected in the BM25B SpLine of the ESRF (European Synchrotron Radiation Facility). The powder sample was introduced in a 1 mm capillary and the wavelength set at 0.82548 Å. The pattern was recorded from 3 to 43° in 2θ (°), with a step of 0.01°, and 2 s per point.

In the initial steps of the refinement, the profile pattern matching analysis allowed us to determine the cell parameters and to refine the profile variables. The structural model obtained for the NiBpaRT compound was used as the starting point of the structural refinement. Rigid bodies were constructed for the pyridyl rings and the ethane groups of the Bpa molecules and for the VO_4 tetrahedra. The bond distances between rigid bodies were restrained to usual values, for example for the linkage between the pyridyl rings and the ethane groups a distance restraint of 1.5 Å with 0.05 sd was imposed, and for the V−O bond distances between VO_4 tetrahedra typical values of 1.7 Å with 0.05 sd were used. First, each rigid body orientation and translation was refined separately until the refinement achieved the convergence. In a second step of the refinement the pyridyl groups were refined jointly. In a last step, all the rigid bodies, including the VO_4 tetrahedra, were refined at the same time.

In that point of the refinement, the rigid bodies of the VO_4 tetrahedra were dissolved and the vanadium and oxygen atoms were refined independently, but introducing several bond distance and angle distance restraints, in order to maintain the general shape of the VO_4 tetrahedra. The bond valence values were checked routinely during the refinement, introducing progressively more chemical logic bond distance restraints. Common isotropic thermal parameters were used for the vanadium and nickel atoms, and for the oxygen, carbon and nitrogen atoms. In the last steps of the refinement, the hydrogen atoms belonging to the Bpa ligand were geometrically introduced, and the angles regarding the linkage between the pyridyl ring and the ethane groups were also restrainted.

The final model possesses short intramolecular H···H contact between symmetrically generated ethane and pyridyl groups. All attempts to get a correct orientation for the ethane groups were unsuccessful. The obtained X-ray powder diffraction data seems to be not good enough to elucidate the final conformation of the ethane groups in the Bpa ligands. Another possibility to explain these short intramolecular H···H contacts is the existence of positional disorder in the ethane groups, but this hypothesis can not be corroborated with the experimental powder pattern. However, just in the initial steps of the refinement, the reorientation of the VO_4 tetrahedra around the Ni cation clearly indicates the transformation mechanism described in this

work, with the incorporation of the V−O terminal oxygen atom to the coordination sphere of the nickel cations. The final fitting is shown in the Supporting Information Figure S1. All the steps of the refinement were carried out with the program JANA.[17]

Physical Measurements. Thermal analyses were performed in air atmosphere, up to 500 °C, with a heating rate of 5 °C min^{-1} on a DSC 2960 Simultaneous DSC-TGA TA Instrument. The temperature dependent PXRD in air atmosphere were realized on a Bruker D8 Advance Vantec diffractometer (CuKα radiation), equipped with a variable-temperature stage (HTK2000) with Pt sample holder. The patterns were recorded each 10 °C from 30 to 500 °C (2θ step = 0.01667°, 2θ range = 5−30°, exposure time = 0.5 s). The temperature variable XRD experiment shows that a structural transformation occurs at temperatures above 180 °C. The reversibility of the solid state reaction was checked heating the sample to 180 °C during ten minutes and recording a XRD pattern. An appraisable color change from green to yellow was observed. The heated sample was then exposed at room temperature checking the color change in time. After ten minutes, the sample recovers its initial color. A XRD pattern was collected after the color recovering. If the heated sample is immersed in ethanol or stored in an anhydrous media, the high temperature compound remains stable.

The physical properties of the room temperature (NiBpaRT) and high temperature (NiBpaHT) compounds were determined. The transformation from NiBpaHT → NiBpaRT is slow enough, and the data acquisition for the IR, Raman, and UV−vis experiments is also short enough, to determine unambiguously the NiBpaHT spectra. To minimize the exposure time to ambient conditions, the sample was heated immediately before the measurements. To determine the magnetic susceptibility of the NiBpaHT compound, the sample was weighted and heated before mounting it in the capsules and measured immediately. The magnetic measurements were carried out in vacuum, preventing the exposure of the NiBpaHT sample to water vapor. The color of the NiBpaHT temperature sample was checked before and after the measurements to ensure that the transformation from NiBpaHT to NiBpaRT did not take place during the data acquisition. Infrared spectra were recorded on a Jasco FT/IR-6100 spectrometer with pressed KBr pellets. IR spectra were obtained for the as synthesized samples, and after heating them to 50, 100, 150, 200, and 250 °C, during one hour. Raman spectra were measured on a Ranishaw Raman confocal microscopy spectrophotometer using the 514 nm laser line for excitation. UV−vis diffuse reflectance spectra were registered on a Varian Cary 5000 spectrophotometer in the 50000−4000 cm^{-1} range. Magnetic measurements on powdered samples were performed in the temperature range 2−300 K, using a Quantum Design MPMS-7 SQUID magnetometer at a magnetic field of 0.1 T.

RESULTS AND DISCUSSION

Structural Analysis. During the structural analysis the comparison between the NiBpaRT and NiBpaHT crystal structures are going to be established. The asymmetric unit of NiBpaRT compound contains two crystallographically independent Bpa organic ligands, two nickel and six vanadium cations, and twenty oxygen atoms. The O(10) and O(21) oxygen atoms lye on special positions at binary axis (Figure 1a). For NiBpaHT, the asymmetric unit contains two oxygen atoms less than in NiBpaRT (Figure 1b).

The 3D crystal structure of NiBpaRT is constructed from four primary building units (PBU), that is, $NiN_2O_3(H_2O)$ octahedra, (V_4O_{12}) cycles, (V_2O_7) dimers, and Bpa organic ligand.[18] Two different secondary building units (SBU) are observed into the crystal structure, the metal−organic $\{Ni(H_2O)(Bpa)\}^{2+}$ chains formed by the connectivity between the nickel cations and the Bpa organic ligands, and the $(V_3O_{8.5})^{2-}$ vanadate chains generated by the linkage between (V_2O_7) dimers and $\{V_4O_{12}\}$ cycles.

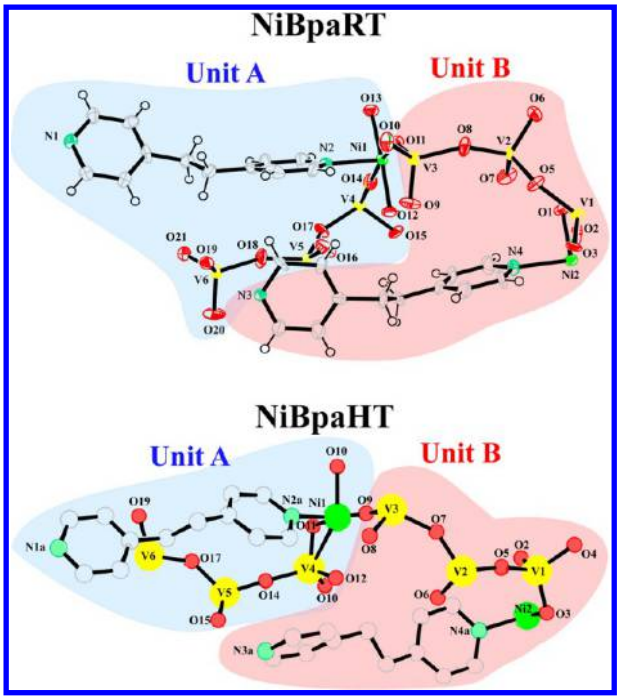

Figure 1. Asymetric Units for NiBpaRT and NiBpaHT.

In NiBpaRT, the coordination sphere of the nickel(II) cations consists of three oxygen atoms, corner linked to vanadium tetrahedra, two nitrogen atoms in trans arrangement, and one coordinated water molecule. The Ni−N bond lengths range from 2.077(4) Å for Ni(1)−N(1) to 2.118(4) Å for Ni(2)−N(4), while Ni−O bond distances range from 2.029(6) Å for Ni(1)−O(13) to 2.132(9) Å for Ni(2)−$O(2)_w$. The minimum and maximum cis angles are 83.5(3) ° for O(1)−Ni(2)−O(2) and 95.8(3) ° for $O(3)^{iv}$-Ni(2)−O(2). The trans angles range from 173.2(3)° ($O(19)^{v}$−Ni(2)−O(2)) to 177.3(3)° ($O(3)^{iv}$−Ni(2)−O(1)) (Supporting Information Table S1). Attending to the bond and angle distances, both the coordination environment of Ni(1) and Ni(2) cations possess near ideal octahedral shape. (Supporting Information Tables S1−S4)

The bond distances for the anhydrous NiBpaHT structural model possess large deviations because of the difficulties to refine such large asymmetric units by powder X-ray diffraction data. Despite that, it is clearly observed that the coordination environment of the Ni(II) cations is highly distorted. The coordination sphere of the nickel atoms after the loss of coordinated water molecules is formed by four oxygen atoms in the equatorial plane and two nitrogen atoms in trans arrangement. Two of the oxygen atoms are linked to the same vanadium atom. This connectivity generates an edge sharing linkage between the nickel octahedron and VO_4 tetrahedron. In fact the long Ni−O bond lengths for Ni(1)−O(12) 2.37(12) Å and Ni(2)−O(2) 2.38(12) Å are related to this connectivity. The other two oxygen atoms are corner shared by two (VO_4) tetrahedral. The cis angles deviates appreciably from their ideal values in a non distorted octahedron, with maximum and minimum values of 79(10)° and 100(7)° for O(10)−Ni(1)−N(1)a and O(9)−Ni(1)−O(12), respectively. The trans angles possess values ranging from 161(5)° for O(3)−Ni(2)−$O(19)^{i}$ (i = x, $-y-1$, $z+1/2$) to 171(6)° for O(9)−Ni(1)−O(11), far from 180°, the value for an ideal octahedron (Supporting Information Table S2).

The V−O bond lengths in NiBpaRT lie within the values observed for previously reported hybrid vanadates. The oxygen atoms corner shared by two adjacent (VO_4) tetrahedra have V−O bond lengths ranging from 1.754(9) Å for V(5)^{ix}−O(15) (ix = $-x$, $-y$, $-z$) to 1.821 Å for V(3)−O(8). The oxygen atoms shared by (VO_4) tetrahedra and $Ni(H_2O)N_2O_3$ octahedra have shorter bond distances, with maximum and minimum values of 1.545(11) Å for V(1)−O(2) and 1.646(8) Å for V(3)−O(11). The four vanadyl V═O bonds present in NiBpaRT crystal structure possess bond lengths ranging from 1.594(11) Å for V(5)−O(17) to 1.632(8) Å for V(6)−O(20) (Supporting Information Table S3). The bond valence calculation,[19] assuming V(V)-O and Ni(II)-O bonds, confirms +5 and +2 charges for vanadium and nickel atoms, respectively (see Supporting Information Table S5).

For NiBpaHT, the V−O bond lengths were restrained during the refinement taking into account the connectivity of the oxygen atom. Despite the high deviation for the obtained values, the bong lengths are in the range of these reported for NiBpaRT. In that regard, the maximum and minimum bond lengths range from 1.84(11) Å for V(1)−O(5) to 1.60(6) Å for V(5)−O(6). The O−V−O angles within the (VO_4) tetrahedra were also restrained, to maintain the tetrahedral geometry of the (VO_4) polyhedra (Supporting Information Table S4). Despite the large deviations of the bond distances and angle values, the bond valence calculations support the obtained chemical model, that is, +2 and +5 valences (see Supporting Information Table S5).

Both in NiBpaRT and in NiBpaHT the six crystallographically independent vanadium atoms are four coordinated. The connectivity between the VO_4 tetrahedra generates $\{V_4O_{12}\}$ cycles and (V_2O_7) dimers. Both PBUs are centrosymmetric, so the $\{V_4O_{12}\}$ cycles are generated by two crystallographically independent VO_4 tetrahedra, and the dimers by one crystallographically independent VO_4 tetrahedron, inverted by a center of symmetry. Into the NiBpaRT and NiBpaHT crystal structures there are two crystallographically independent $\{V_4O_{12}\}$ cycles and (V_2O_7) dimers, formed by the V(1), V(2), and V(3) and V(4), V(5), and V(6) atoms, respectively. So, there are two crystallographically independent vanadate chains and two crystallographically independent $\{Ni(H_2O)(Bpa)\}^{2+}$ metal−organic chains. Hereafter, the vanadate chains constructed by the $V(1)O_4$, $V(2)O_4$, and $V(3)O_4$ tetrahedra, and these ones formed by the $V(4)O_4$, $V(5)O_4$, and $V(6)O_4$ tetrahedra are going to be named as V(A) and V(B) vanadate chains, respectively. Similarly, the metal−organic chains containing the Ni(1) and Ni(2) cations are going to be named as Ni(A) and Ni(B) metal−organic chains. The main difference between these crystallographically pseudoequivalent units arises in the opposite orientations of the ethane groups and (V_2O_7) dimers, belonging to the Bpa organic ligand in Ni(A) and Ni(B) metal−organic chains and V(A) and V(B) metavanadate chains.

Figure 2 shows the connectivity between the $\{V_4O_{12}\}$ cycles, (V_2O_7) dimers and the nickel cations within the V(A) chains. In each cycle, the $V(1)O_4$ tetrahedron is corner linked with two $V(2)O_4$ tetrahedra within the cycle, and to two $Ni_2(H_2O)N_2O_3$ octahedra. The $V(2)O_4$ polyhedra connects the cycle with the (V_2O_7) dimers, giving rise to a one-dimensional vanadate chain. The (V_2O_7) dimers are generated by two corner linked $V(3)O_4$ tetrahedra related by a center of symmetry. Both the $V(2)O_4$ and $V(3)O_4$ polyhedra possess nonbonded oxygen atoms. In the case of the terminal oxygen atoms belonging to the $V(3)O_4$ tetrahedra, these plays very important role in the structural transformation because of the loss of coordinated water molecules. The connectivity of the $\{V_4O_{12}\}$ cycles and (V_2O_7) dimers in the V(B) chains is equivalent to that one of the V(A) chains.

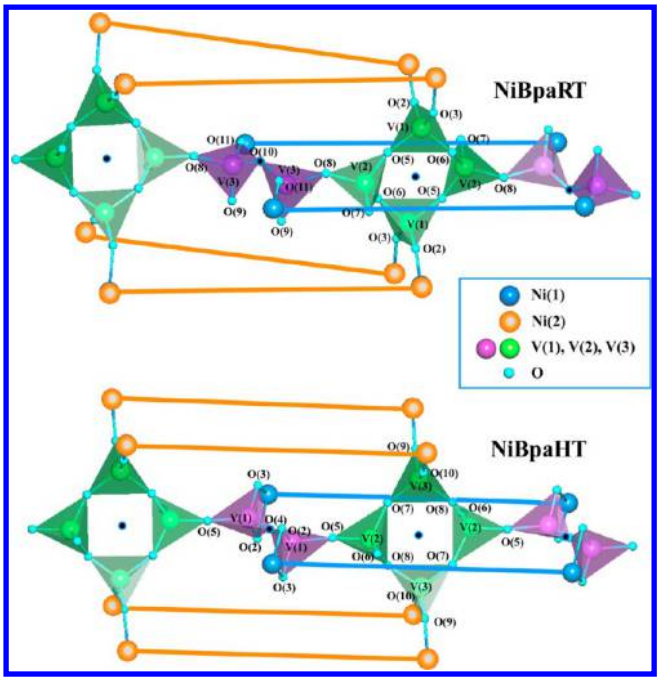

Figure 2. Connectivity between the vanadate chains and the metal−organic chains in NiBpaRT and NiBpaHT. The Bpa organic ligands have been simplified as cylinders.

In comparison with NiBpaRT, in NiBpaHT, the vanadium oxide primary building blocks remain practically unchanged. Slight reorientations of the (VO_4) tetrahedra belonging to the (V_2O_7) dimers and $\{V_4O_{12}\}$ cycles are observed, being the most important change, the rotation of the (VO_4) tetrahedra within the (V_2O_7) dimers to edge share the NiN_2O_4 octahedron in NiBpaHT, after the loss of coordinated water molecules (Figures 2 and 8).

In Figure 2, the connectivity between the V(A) vanadate chains and the metal−organic chains is also observed. Each vanadate chain acts as a six directional connector, linking four Ni(A) metal−organic chains through the $\{V_4O_{12}\}$ cycles and two Ni(B) metal−organic chains across the (V_2O_7) dimers (Figure 2).

In fact, as in natural pyroxenes, the crystal structures of NiBpaRT and NiBpaHT can be described as the stacking sequence of crystallographically nonequivalent hybrid chains with different orientation of their tetrahedra. (Figure 3a.1, a.2, and b). The connectivity between the Ni(A) and V(A), and Ni(B) and V(B) chains, generates the inorganic−organic NiV(A) and NiV(B) chains simplified in the Figure 3a.1 and a.2. Each NiV(A) chains connect with the nickel cations of four NiV(B) chains through the $\{V_4O_{12}\}$ cycles, giving rise to a three-dimensional inorganic−organic framework, and also to a three-dimensional inorganic substructure. Figure 3b simplifies the stacking of the NiV(A) and NiV(B) chains along the [100] direction.

The existence of two pseudoequivalent units is related to the systematic twining and diffuse scattering in NiBpaRT. It is difficult to determine exactly what is the origin of the systematic twining of the crystals, observed independently of the synthetic

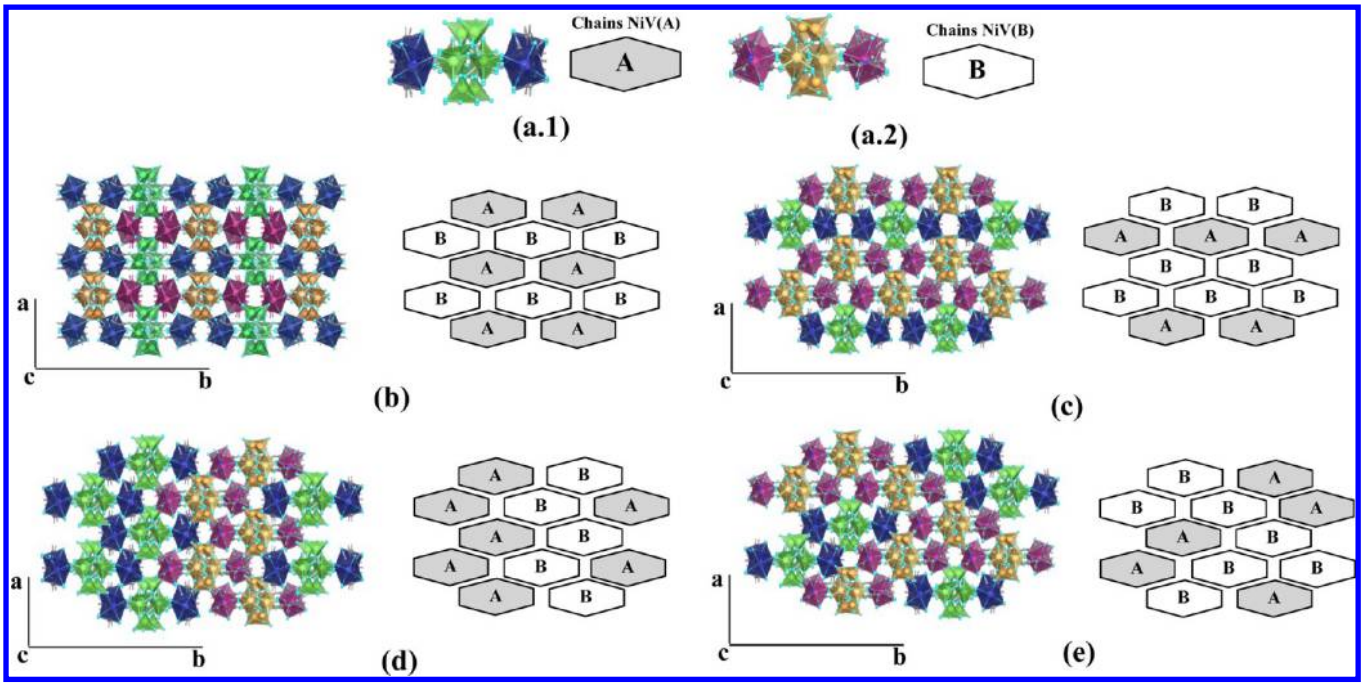

Figure 3. Simplified view of the NiV(A) and NiV(B) hybrid chains. The blue and magenta polyhedra represent the Ni(A) and Ni(B) metal−organic chains, while the green and orange subunits are the V(A) and V(B) metavanadate chains. (b) Crystal structure of NiBpaRT. The simplified stacking of the crystallographically independent units in the average crystal structure is also represented. Possible local disorder or stacking faults of the NiV(A)−NiV(B) crystallographically pseudoequivalent hybrid chains along the (c) [100], (d) [010], and (e) randomly disordered.

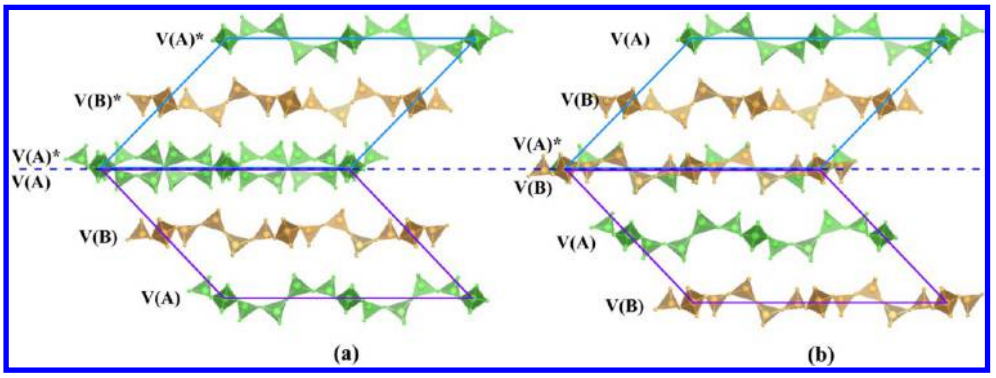

Figure 4. Vanadate chains stacking along the [100] direction. Possible stacking sequences in the twin frontier (a) V(A)−V(B)−V(A)−V(A)*−V(B)*−V(A)* and (b) V(B)−V(A)−V(B)−V(A)*−V(B)*−V(A)*.

conditions, but under our point of view is related to the crystal structure itself. The twin law (1 0 1, −0 1 0, 0 0 −1) indicates that the twining is ascribed to the stacking of the chains along the [100] direction. Figure 4 represents the stacking of the V(A) and V(B) vanadate chains along the [100] direction. If the ABABAB stacking sequence is maintained in the twinning frontier, the mismatch between the V(A) and V(A)* chains is evident (Figure 4a). Another possibility is to introduce a stacking fault in the twin frontier. In the V(B)−V(A)−V(B)−V(A)*−V(B)*−V(A)* sequence shown in the Figure 4b, the similarity between the V(A)* and V(B) chains suggests that the twining of the crystals does not involve a great energy barrier. So the crystals are easily twinned perpendicular to the stacking direction of the chains.

During the crystal data reduction an important contribution of the diffuse scattering was detected in the recorded pictures. Some of the diffraction maxima possess suspicious and irregular shapes, and there is diffuse intensity located along the diffraction rings connecting the diffraction maxima (Figure 5). Radial diffuse component is detected in several diffraction maxima, and diffuse streaks are observed along the a^* and c^* directions (see Figure 5: (1kl) and (hk2) projections). But the stronger diffuse components are detected in the (hkl) planes, when k is odd (Figure 5). In the (h3l) and (h5l) planes, there are short diffuse streaks in the ⟨101⟩ directions, and also diffuse halos are observed.

Any departure from a strictly long-range-ordered average structure give rise to diffuse scattering of crystals.[20] The origin of the diffuse scattering in the studied compound is ascribed to two different levels of disorder or departures from average structure, disorders of crystallographically pseudoequivalent NiV(A) and NiV(B) chains, and local disorder of the primary building units. One of the possible reasons for the diffuse scattering associated to the long-range order deviations is the disorders of NiV(A) and NiV(B) chains. Qualitatively, the different alternatives are analyzed in Figure 3c−e. The average structure is described as the ABABAB stacking of the A and B chains along the [100] direction (Figure 3 b). Taking into

dx.doi.org/10.1021/cg401540s | Cryst. Growth Des. 2014, 14, 658−670

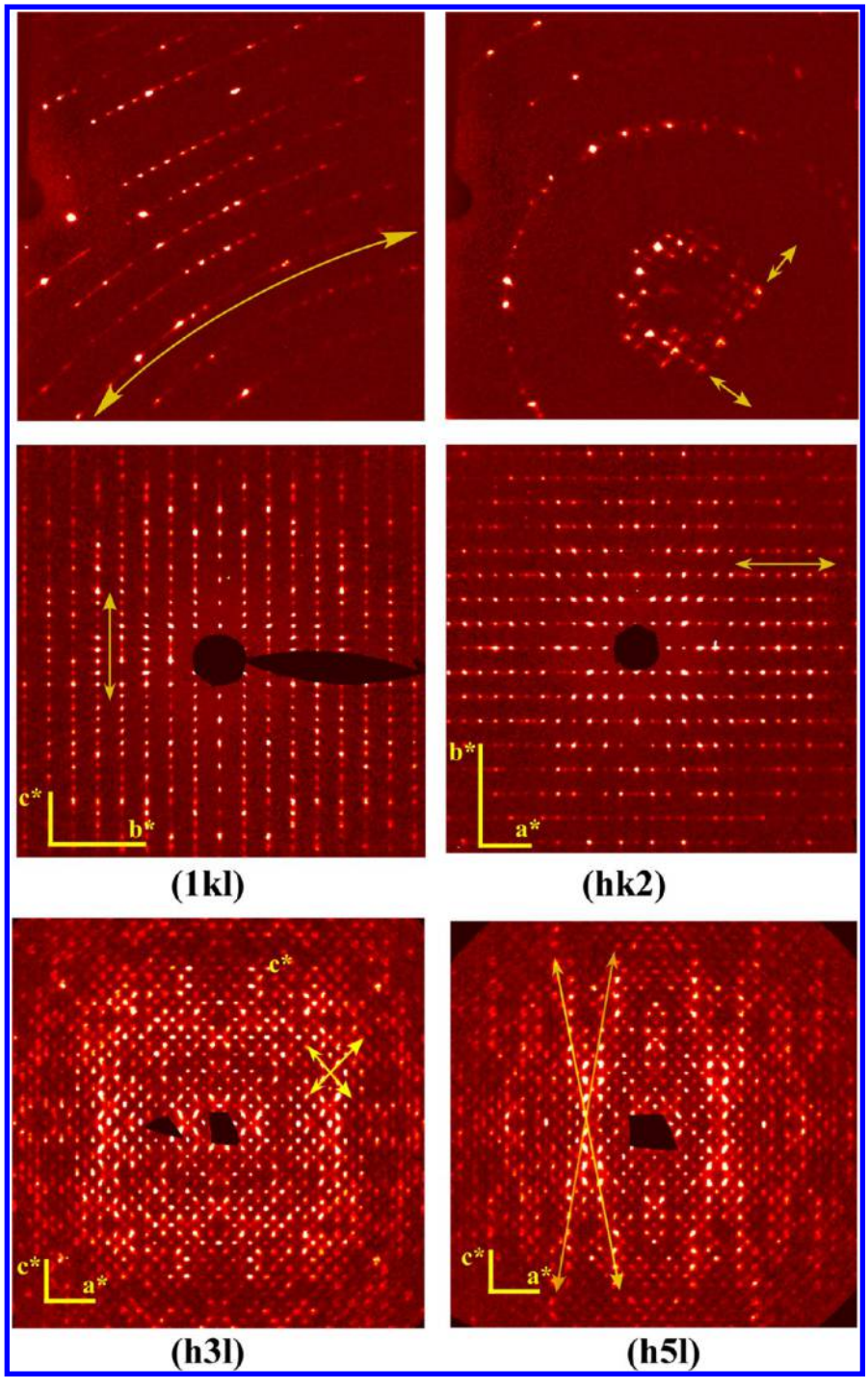

Figure 5. Diffuse scattering along the diffraction rings, in the diffraction maxima, diffuse streaks along the [100], [001], and [101] directions, and diffuse halos detected on the (*h*3*l*) and (*h*5*l*) planes.

account that the diffuse scattering is given principally in the *a** and *c** directions, the most plausible origin could be the existence of stacking faults or stacking disorders along the [100] direction. In this sense, Figure 3c illustrates a crystal structure with a local AABAB stacking of the hybrid chains along [100]. Nevertheless, the disorder of the NiV(A)−NiV(B) pseudoequivalent units, in principle could be also along the [010] direction (Figure 3d), or in the most complex case, the hybrid chains could be randomly disordered (Figure 3e). Whatever the type of local disorder, the exchange of NiV(A) for NiV(B) chains will produce local strain that has to be solved by the distortion or reorientation of the (VO_4) tetrahedra and the pyridyl and ethane groups belonging to the Bpa organic ligand. So, the observed diffuse scattering along the [100], [001], and [101] directions could be related to the disorder or stacking faults of the NiV(A) and NiV(B) pseudoequivalent chains, while the diffuse halos could be ascribed to the local distortion and reorientation of the organic ligand and (VO_4) polyhedra near the disordered environments.

The NiBpaRT and NiBpaHT crystal structures can be topologically described as self-catenated three nodal (4-c)(5-c)(6-c) connected nets, with $\{4.5^6{\cdot}6^2{\cdot}8\}_2\{4^2{\cdot}5^9{\cdot}6^4\}\{5^5{\cdot}6\}$ point

symbol (Figure 6a). This description considers (i) the $\{V_4O_{12}\}$ cycles as a (6-c) node connecting four nickel octahedra

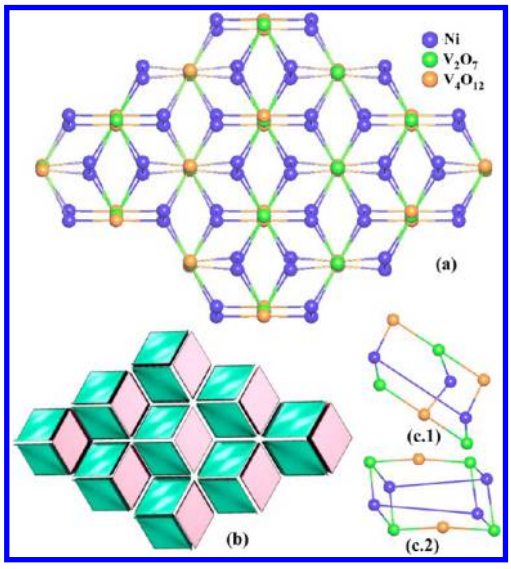

Figure 6. (a) Three nodal (4-c)(5-c)(6-c) connected self-catenated net. (b) Natural tiling of the net. (c.1) and (c.2) $[5^2.6^2]$ and $[4^2.5^4]$ tiles, respectively.

belonging to the metal−organic chains, and two (V_2O_7) dimers within the metavanadate chains, (ii) the nickel octahedra as a (5-c) node, sharing two nickel nodes within the same metal−organic chains through the Bpa organic linkers, two $\{V_4O_{12}\}$ cycles and one (V_2O_7) dimer, and (iii) the (4-c) nodes related to the (V_2O_7) dimers that links two $\{V_4O_{12}\}$ cycles within the metavanadate chains and two nickel octahedra of the metal−organic chains. As in many hybrid vanadates, the simplified net is a new self-penetrated topology.[21] The analysis of the shortest rings allows the calculation of the natural tiling of the net (Figure 6b). The tiling is constructed from two different tiles, $[5^2{\cdot}6^2]$ (Figure 6 c.1 and green polyhedra in Figure 6b) and $[4^2{\cdot}5^4]$ (Figure 6 (c.2) and pink polyhedra in Figure 6b).

Physicochemical Properties. *Thermal Properties and Structural Transformation.* The increase of temperature upon 175 °C generates a single crystal to powder solid state transformation with an appraisable color change of the sample. The TG/DSC curves indicate that the structural transformation is related to the loss of the water molecules coordinated to the nickel(II) metal centers (Supporting Information Figure S2). In fact, the thermogravimetric curve shows two weight losses of 3.04% (100−175 °C) and 31.30% (350−480 °C) associated to the release of two coordinated water molecules (calcd 3.22%) and the calcination of two Bpa organic ligands per formula unit (32.61%). The thermodiffractometry reveals the instability of the initial phase and the generation of a new crystalline compound between 120 and 175 °C (Figure 7) in good agreement with the release of the coordinated water molecule from the nickel cation coordination environment. Figure 7 shows the generation of the diffraction maxima associated to the structural transformation from NiBpaRT to NiBpaHT.

Taking the NiBpaRT crystal structure as a starting point, the crystal framework after the loss of the coordinated water molecules (NiBpaHT) was obtained by a rigid body Rietveld refinement. The solid state transformation mechanism involves the terminal oxygen atoms of the (VO_4) tetrahedra belonging to the $\{V_2O_7\}$ dimers. The removal of the bonded water

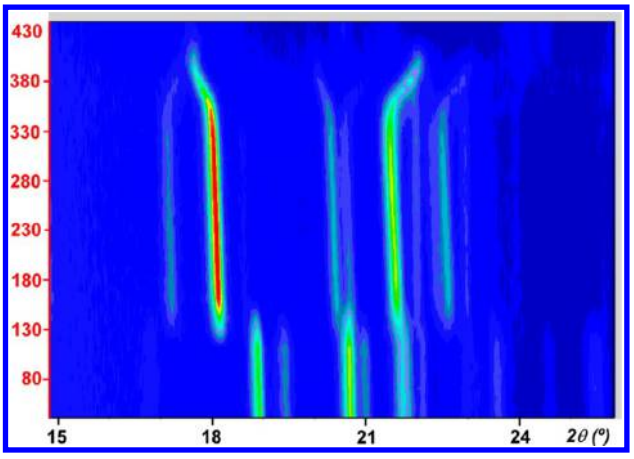

Figure 7. Selected 2θ (°) interval of the thermodiffractometry. The solid state transformation of NiBpaRT to NiBpaHT takes places between 120 and 180 °C.

molecules from the coordination environment of the Ni(II) cations generates the rotation of the (VO_4) tetrahedra, bringing closer the terminal oxygen atom to the Ni(II) cation (Figure 8).

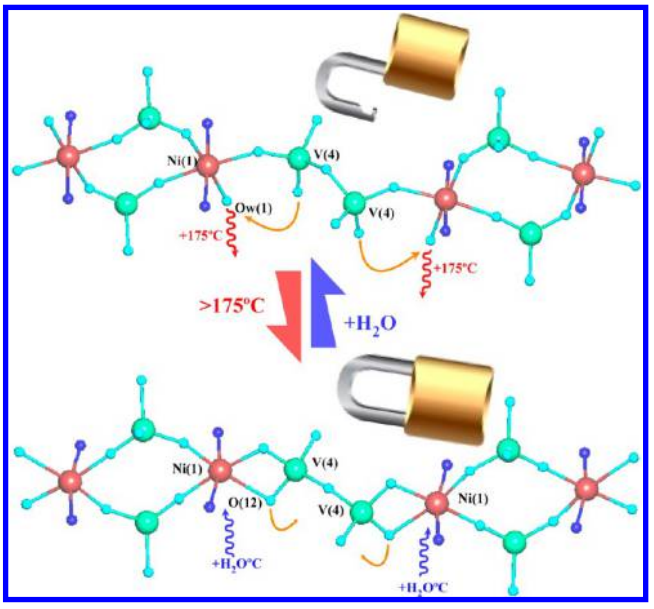

Figure 8. Generation of new Ni−O bonds in the padlock mechanism of the solid-state transformation of NiBpaRT to NiBpaHT. The solid state reaction mechanism is the same for the A and B crystallographically independent units. For simplicity, only the transformation mechanism of the A units is shown.

In this way, the crystal structure self-complete the octahedral coordination sphere of the Ni(II) cation generating new Ni−O bonds (2.37(12) Å for Ni(1)−O(12), and 2.38 (12) Å for Ni(2)−O(2)). Nonetheless, the nickel coordination sphere is severely distorted because in NiBpaHT the NiN_2O_4 octahedra and (VO_4) tetrahedra share one edge, and the Ni−O bond distances and O−Ni−O angles take values far from those observed in NiBpaRT structure.

The solid-state structural transformation does not only involve this padlock mechanism (Figure 8), but there are also slight readjustment in the orientation of the (V_2O_7) dimers and $\{V_4O_{12}\}$cycles and in the pyridyl rings and ethane groups belonging to the Bpa organic ligands. The weak interactions

Table 2. Crystal Data and Structure Refinement for NiBpaHT

compound	NiBpaHT
formula	$C_{24}H_{24}N_4Ni_2O_{17}V_6$
fw (g/mol)	1063.5
cryst syst	monoclinic, *P*
color	green
space group, no.	*P*2/*c*, 13
a (Å), *b* (Å), *c* (Å)	19.056(9), 9.7904(15), 26.613(7)
β (deg)	134.35(2)
Z, *F*(000), *T* (K)	4, 2104, 453
μ (mm^{-1})	3.94
cryst size (mm)	powder
synchrotron radiation (*λ*(Å))	0.82548
no. of points	4001
2*θ* (deg) interval	3−43
params/restraints	119/106
R1[a]	0.0658
wR2/wR2[a] expected	0.0903/0.1782
GOF	0.510

[a] $R1 = (\sum w||F_0| - |F_c||)/(\sum w|F_0|)$. $wR2 = ((\sum w((F_0)^2 - (F_c)^2)^2)/((\sum w((F_0)^2)^2)^{1/2}$. $GOF = ((\sum w((F_0)^2 - (F_c)^2)^2)/((n-p))^{1/2}$.

between the coordinated water molecules and the VO_4 tetrahedra involved in the padlock mechanism could play an important role during the transformation process. The hydrogen bonds between the coordination water molecules and adjacent atoms could not be calculated because of the impossibility to locate the hydrogen atoms by X-ray diffraction. But the distances between the oxygen atoms of the coordinated water molecules and the adjacent terminal oxygen atoms belonging to the V═O vanadyl bonds are short enough for the existence of possible hydrogen bonding (Table 3). In fact, the

Table 3. Possible Hydrogen Bonds Established between the Coordinated Water Molecules and Adjacent Oxygen Atoms

donor	acceptor	donor−acceptor distance (Å)
Ni(1)−O(12)	O(9)═V(3)	2.736
Ni(1)−O(12)	O(17)═V(5)	2.828
Ni(2)−O(1)	O(20)−V(6)	2.723
Ni(2)−O(1)	O(7)−V(2)	2.862

shortest distances are established with the terminal oxygen atoms belonging to the VO_4 tetrahedra within the V_2O_7 dimers, directly involved in the structural transformation process. This fact suggests that the incorporation of the terminal oxygen atoms of the VO_4 tetrahedra into the coordination sphere of the nickel cations could be guided by the existence of previous hydrogen bonding between the coordinated water molecules and the vanadyl groups.

The structural transformation gives rise to a reduction of 105 $Å^3$ unit cell volume ($V_{100°C}$ = 3626.6(9) $Å^3$ → $V_{150°C}$ = 3521(1) $Å^3$) (Supporting Information Figure S3). It is noticeable that the volume loss of 105 $Å^3$ is near the theoretical volume of two water molecules of 80 $Å^3$. The cell parameters behave different during the solid state transformation, the main changes are ascribed to the "*a*" and "*b*" parameters with a reduction and increase of −3.14% ($a_{100°C}$= 19.566(3) Å → $a_{150°C}$ = 18.951(4) Å) and +3.97% ($b_{100°C}$= 9.388(1) Å → $b_{150°C}$ = 9.761(1) Å), respectively. The contraction of the *a* parameter is related to the formation of new edge sharing connectivity between the nickel octahedra and (VO_4) tetrahedra, while the increase of the *b* parameter is given by a slight reorganization of the metal−organic and metavanadate chains along the [010] direction.

A great number of molecular compounds with structural transformations due to the loss of coordinated water molecules have been reported. In the case of the studied compound, the reduction of the cell volume is related to the reorganization of the primary and secondary building units within the crystal structure to compensate the coordination environment of the nickel metal centers after the loss of the coordinated water molecules. For example, for the previously reported $[Co_2(ppca)_2(H_2O)(V_4O_{12})_{0.5}]$ hybrid vanadate, the loss of the coordinated water molecules gives rise to a change in the coordination environment of the cobalt metal centers from an octahedral coordination sphere to a five coordination one. The 30 $Å^3$ volume reduction is less than the volume of free H_2O water molecule (40 $Å^3$), and is ascribed also to the structural reorganization after the loss of coordinated water molecules.

As judged by the X-ray powder diffraction patterns, the transformation is completely reversible (Supporting Information Figure S4). NiBpaHT is transformed to NiBpaRT in ten minutes under room temperature conditions, and immediately if the sample is soaked in water. This fact can be easily understandable taking into account that the coordination environment of the nickel atoms in the high temperature crystal structure is highly distorted, so the cations tend to incorporate coordination water molecules in order to recover the regular and non strained coordination environment of the room temperature crystal structure. This padlock mechanism is similar to that observed in coordination polymers in which the bonding of the unused donor atoms of the already attached ligands next to the metal center takes place, as it occurs in several coordination polymers constructed from carboxylates.[22] However, the solid state transformations involving nonbonded atoms and mobile polyhedra of the inorganic skeleton are less common. The edge sharing connnectivity between the nickel octahedra and (VO_4) tetrahedra is not commonly observed in hybrid compounds. Moreover, there is only one example of hybrid vanadate with the metal center edge shared to the (VO_4) tetrahedra,[23] and in transition metal phosphates is also rarely observed.[24]

Spectroscopic Properties. The UV−vis spectra of NiBpaRT and NiBpaHT show the characteristic absorption bands for octahedrally coordinated high spin Ni(II) d^8 cations (Supporting Information Figure S5), attributed to the $^3A_{2g} \rightarrow {}^3T_{2g}$ (NiBpaRT = 15780 cm^{-1}, NiBpaHT = 15150 cm^{-1}) and $^3A_{2g} \rightarrow {}^3T_{1g}$ (NiBpaRT = 9680 cm^{-1}, NiBpaHT = 9250 cm^{-1}) allowed transitions. The UV−vis spectra confirm the octahedral coordination environment of the nickel cations in the NiBpaHT crystal structure. Variations in the absorption and shifts to lower wavelength values are observed for the maxima during the solid state transformation, in good agreement with the color change.

The IR and Raman spectra for the NiBpaRT and NiBpaHT show the characteristic absorption bands of the metavanadate groups and Bpa organic ligand. Three main regions can be distinguished: (i) the absorption maxima related to the crystallization and coordinated water molecules (3700−3000 cm^{-1}), (ii) the Bpa ligand vibrational modes generating absorption maxima in the 1700−1000 cm^{-1} range, and (iii) the absorption bands located at frequencies below 1000 cm^{-1}, associated to $\{V_4O_{12}\}$ cycles and (V_2O_7) dimers, and tentatively

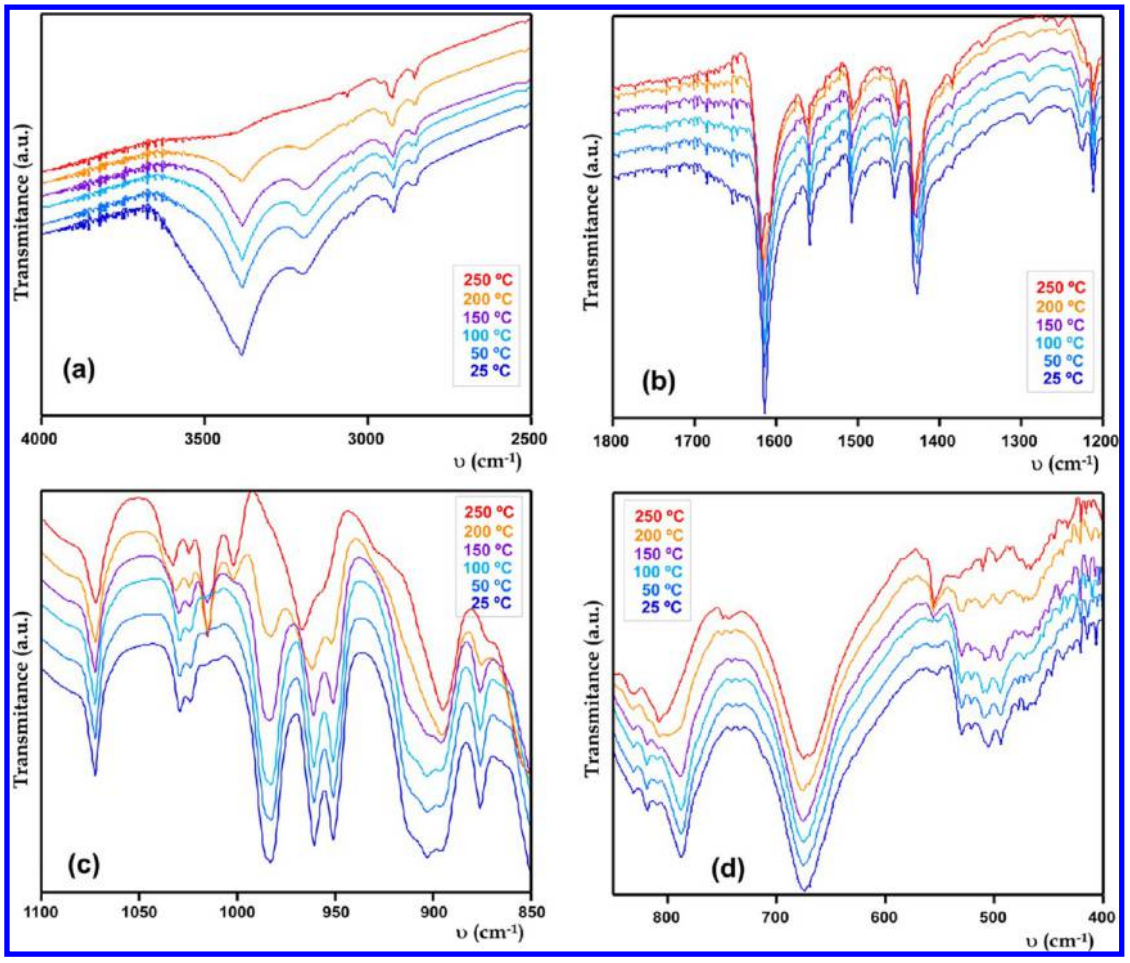

Figure 9. IR spectra of the sample heated at different temperatures during 20 min. (a) IR wavelength range associated to the stretching vibration of the O−H groups. (b) Absorption bands related to the Bpa organic ligand. (c) 1050−1000 cm^{-1} δ(ring). 1000−900 cm^{-1} V═O vanadyl stretching vibration. (d) 850 −800 cm^{-1} $\upsilon_{as}(VO_4)$ groups vibrations. 690 cm^{-1} υ_{as}(V−O−V) and υ_{as}(V−O−Ni) vibrations.

assigned to the V═O stretching (1020−950 cm^{-1}), $\upsilon_{as}(VO_4)^{-3}$ (890 cm^{-1}) and υ_{as}(V−O−V) 800−600 cm^{-1} vibrations. In the Raman spectra, the low Raman shift interval (600−140 cm^{-1}) contains also the vibrational information about the Ni−O, Ni−py, and Ni−H_2O bonds.[25] The evolution of the most representative absorption bands are depicted in the Figure 9 and Supporting Information Figure S6. The IR and Raman spectra show important changes in the position and intensity of the absorption bands related to the stretching vibration of V═O bonds (Figure 9c). This fact is in good agreement with the participation of the terminal oxygen atoms within the (V_2O_7) dimers in the generation of new Ni−O bonds after the loss of coordinated water molecules.

Regarding the absorption bands related to the Bpa organic ligand, these are slightly modified after the transformation. This observation is in good agreement with the determined high temperature structural model in which only slight reorientation of the Bpa organic ligands is observed during the solid state reaction (Figure 9b). In the IR spectra, the loss of coordinated water molecules also generates an intensity decrease of the absorption bands related to the stretching vibration of the O−H bonds (Figure 9a). The absorption bands related to the $\upsilon_{as}(VO_4)$ and υ_{as}(V−O−V) vibrational modes remain approximately unchanged, indicating that the VO_4 tetrahedra and V−O−V linkages are slightly affected by the solid state transformation (Figure 9c and d).

Magnetic Properties. Magnetic measurements were performed on powdered samples from room temperature to 2 K, at a magnetic field of 0.1 T. The thermal evolution of $\chi_m T$ vs T for NiBpaRT and NiBpaHT are shown in Figure 10. A maximum in $\chi_m T$ product is observed at 8 and 10 K for NiBpaRT and NiBpaHT respectively. The $\chi_m T$ values at 300 K

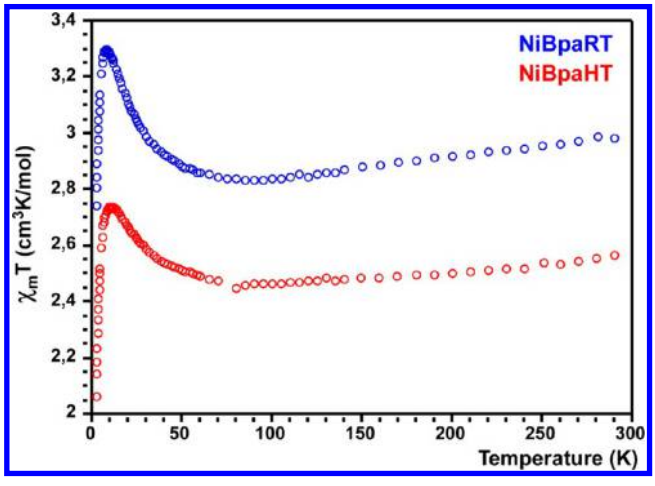

Figure 10. Thermal evolution of χ_m curves for NiBpaRT and NiBpaHT.

per nickel(II) atom are 1.43 cm^3K/mol and 1.25 cm^3K/mol, for NiBpaRT and NiBPaHT. These ones are in the same range that the value for an isolated $S = 1$ ion ($\chi_m T$ = 1.21 cm^3K/mol g = 2.2). The $\chi_m T$ vs temperature curves for NiBpaRT and NiBpaHT show a continuous increasing of its value in the 300−8 K and 300−10 K temperature ranges, respectively. At lower temperatures, the $\chi_m T$ value decrease abruptly.

As the shortest distance Ni···Ni across the Bpa ligand is 13.40 Å and 13.30 Å for NiBpaRT and NiBpaHT, respectively, the overall magnetic interaction should be mainly attributed to the superexchange coupling within the inorganic framework. The connectivity between the Ni(II) metal centers across O−V−O atoms suggests the existence of dimeric magnetic units (Figure 8). The distance between the nickel centers in the dimeric units is of 5.34 and 5.54 Å for NiBpaRT and NiBpaHT, and this magnetic pathway J1 involves five atoms Ni−O−V−O−Ni. The adjacent dimers are linked through (V_2O_7) dimers (J2: 9.35 Å for NiBpaRT and 8.29 Å for NiBpaHT), and {V_4O_{12}} cycles (J3: 9.40 Å for NiBpaRT and 9.79 Å for NiBpaHT). In principle, the distance between the adjacent dimers, and the number of atoms involved in the J2 and J3 magnetic pathways, are very large for an effective interdimer magnetic coupling.

Therefore, the thermal evolution of the $\chi_m T$ curve is ascribed to the magnetic interaction within the dimeric units. The intradimer antiferromagnetic interaction can be treated with the isotropic spin Hamiltonian $H = -2JSASB$. The molar magnetic susceptibility for a Ni(II) dimer (local spins SA = SB = 1) may be expressed by eq 1:

$$\chi_m = \frac{2N\beta^2 g^2}{kT}\frac{1 + 5\exp(4x)}{3 + 5\exp(4x) + \exp(-2x)} + \mathrm{TIP}$$
$$x = J/kT \qquad (1)$$

where N is Avogadro's number, β is Bohr magneton, g is gyromagnetic ratio, k is Boltzmann constant, T is absolute temperature, and TIP is temperature-independent paramagnetism. The best fitting parameters obtained between 300 and 20 K are J/k = 2.78(4) K, g = 2.298(2), TIP = 0.00111(2) cm^3K/mol for NiBpaRT and J/k = 2.25(5) K, g = 2.162(2), TIP= 0.00067(2) cm^3K/mol for NiBpaHT. These values are consistent with intradimer ferromagnetic interactions. Probably, below the temperature of the $\chi_m T$ maxima J2 and J3 magnetic exchange pathways gains importance, and an antiferromagnetic coupling is established between the adjacent dimeric units, giving rise to the observed decreasing in the $\chi_m T$ curve.

It is not surprising that the magnetic coupling between the nickel metal centers in NiBpaRT and NiBpaHT is so similar, because the connectivity into the dimeric units and between the dimeric units is maintained after the structural transformation. The main difference between the magnetic behavior of both compounds is the g value obtained from the magnetic fitting. Probably, the explanation for the difference between the g values of NiBpaRT and NiBpaHT crystal structures is the distortion degree of the nickel coordination environments, after the structural transformation.

CONCLUSIONS AND DISCUSSION

The diffuse scattering observed in the diffraction images could be ascribed to local disorders of the two crystallographically independent and pseudoequivalent hybrid chains of the NiBpaRT crystal structure. These local disorders give rise also to rearrangements of the Bpa organic ligands and VO_4 tetrahedra, belonging to the metal−organic and metavanadate chains, which could also contribute to the diffuse scattering. Moreover, the systematic (1 0 1, 0 −1 0, 0 0 1) twining of the single crystals, can be clearly related to the stacking of the A and B layers along the [100] direction.

The loss/uptake of coordinated water molecules in NiBpaRT induces a reversible solid state transformation. The coordination environment of the Ni(II) cations is completed by the incorporation of the terminal oxygen atoms belonging to the adjacent VO_4 tetrahedra, through the generation of a new Ni−O bond. The IR and Raman spectra confirm that there are drastic changes in the vanadyl terminal group during the loss of bonded water molecules, while the UV−vis spectra confirms the octahedral coordination environment of the Ni(II) cation in the high temperature crystal structure. To the best of our knowledge, this is the first reversible solid state mechanism involving only polyhedra within the inorganic-substructure of inorganic−organic materials.

Up to now, the previous studies of solid state transformations in hybrid vanadates report a great loss of crystallinity during the loss of bonded water molecules. But, these studies have been carried out in hybrid vanadates constructed from rigid dipodal ligands. The rational design of the crystal structures, and more specifically, the rational choice of initial structural building blocks with enough degree of freedom to establish new weak interactions and/or bonds is a essential task to avoid the crystalline to pseudoamorphous transformations after the loss of coordinated species. In that regard, different possible strategies can be adopted, such as (i) the synthesis of crystal structures containing not rigid inorganic substructures formed by corner-sharing polyhedra, (ii) the choice of secondary metal centers that could adopt different coordination environments, such as Co(II) and Cu(II), and (iii) the use of flexible organic ligands, instead of Bpe, that not only could reorient itselves or adopt different conformations, but may also incorporate not bridging atoms to the coordination sphere of the secondary metal centers.

ASSOCIATED CONTENT

Supporting Information

Rietveld refinement of NiBpaHT, TG and DSC curves, thermal evolution of the cell parameters during the structural transformation, transformation reversibility, UV−vis spectra, Raman spectra, magnetic exchange pathways, magnetic fittings, selected bond distances (Å), selected angles (deg), bond valence sum, and crystallographic information files. This information is available free of charge via Internet at http://pubs.acs.org/.

AUTHOR INFORMATION

Corresponding Author

*E-mail: maribel.arriortua@ehu.es. Phone: 34-946012534. Fax: 34-946013500.

Notes

The authors declare no competing financial interest.

ACKNOWLEDGMENTS

This work has been financially supported by the "Ministerio de Ciencia e Innovación" (MAT2010-15375) and the "Gobierno Vasco" (IT630-13), which we gratefully acknowledge. The authors thank the technicians of SGIker (UPV/EHU) financed by the National Program for the Promotion of Human

Resources within the National Plan of Scientific Research, Development and Innovation, "Ministerio de Ciencia y Tecnología" and "Fondo Social Europeo" (FSE). The authors thank to the Spanish BM25B beamline, and ESRF (European Synchrotron Radiation Facility), for the measurement time. R.F.d.L. thanks the MICINN (Madrid, Spain) for funding. E.S.L. and J.O. thank the UPV/EHU for funding.

REFERENCES

(1) (a) Kole, G. K.; Vittal, J. J. *Chem. Soc. Rev.* **2013**, *42*, 1755−1775. (b) Georgiev, I. G.; MacGillivray, L. R. *Chem. Soc. Rev.* **2007**, *36*, 1239−1248. (c) Vittal, J. J. *Coord. Chem. Rev.* **2007**, *251*, 1781−1795. (d) Garcia-Caribay, M. A. *Acc. Chem. Res.* **2003**, *36*, 491−498. (e) Coronado, E.; Gimenez-Marques, M.; Minguez Espallargas, G. *Inorg. Chem.* **2012**, *51*, 4403−4410. (f) Kole, K. G.; Peedikakkal, A. M. P.; Toh, B. M. F.; Vittal, J. J. *Chem.—Eur. J.* **2013**, *19*, 3962−3968. (g) Zheng, S.-L.; Wang, Y.; Yu, Z.; Lin, Q.; Coppens, P. *J. Am. Chem. Soc.* **2009**, *131*, 18036. (h) Michaelides, A.; Skoulika, S.; Siskos, M. G. *Chem. Commun.* **2011**, *47*, 7140−7142. (i) Nagarathinan, M.; Vittal, J. J. *Chem. Commun.* **2008**, 438−440.

(2) (a) Calderon-Casado, A.; Barandika, G.; Bazan, B.; Greaves, M. K.; Vallcorba, O.; Rius, J.; Miratvittles, C.; Arriortua, M.-I. *CrystEngComm* **2011**, *13*, 6831−6838. (b) Arriortua, M. I.; Barandika, M. G.; Bazan, B.; Calderon-Casado, A.; Urtiaga, M. K. WO 2013057350 A1 20130425, 2013. (c) Orive, J.; Larrea, E. S.; Fernández de Luis, R.; Iglesias, M.; Mesa, J. L.; Rojo, T.; Arriortua, M. I. *Dalton Trans.* **2013**, *42*, 4500−4512.

(3) (a) Mahata, P.; Draznieks, C.-M.; Roy, P.; Natarajan, S. *Cryst. Growth Des.* **2013**, *13*, 155−168. (b) Kondo, A.; Nakagawa, T.; Kajiro, H.; Chinen, A.; Hattori, Y.; Okino, F.; Ohba, T.; Kaneko, K.; Kanoh, H. *Inorg. Chem.* **2010**, *49*, 9247−252. (c) Duan, Z.; Zhang, Y.; Zhang, B.; Zhu, D. *J. Am. Chem. Soc.* **2009**, *131*, 6934−6935. (d) Du, M.; Li, C.-P.; Wu, J.-M.; Guo, J.-H.; Wang, G.-C. *Chem. Commun.* **2011**, *47*, 8088−8090. (e) Wen, L.; Cheng, P.; Lin, W. *Chem. Commun.* **2012**, *48*, 2846−2848.

(4) (a) Li, H.; Eddaoudi, M.; ÓKeeffe, M.; Yaghi, O. M. *Nature* **1999**, *402*, 276−279. (b) Rosi, N. L.; Kim, J.; Eddaoudi, M.; Chen, B.; ÓKeeffe, M.; Yaghi, O. M. *J. Am. Chem. Soc.* **2005**, *127*, 1504−1518. (c) Chen, S.-C.; Zhang, J.; Yu, R.-M.; Wu, X.-Y.; Xie, Y.-M.; Wang, F.; Lu, C.-Z. *Chem. Commun.* **2010**, *46*, 1449−1451.

(5) (a) Oliver, S.; Kuperman, A.; Lougha, A.; Ozin, G. A. *Chem. Mater.* **1996**, *8*, 2391−2398. (b) Riou, D.; Roubeau, O.; Férey, G. *Z. Anorg. Allg. Chem.* **1998**, *624*, 1021−1025. (c) Román, P.; San José, A.; Luque, A.; Gutiérrez-Zorrilla, J. M. *Inorg. Chem.* **1993**, *32*, 775−776. (d) Berrocal, T.; Mesa, J. L.; Pizarro, J. L.; Bazán, B.; Lezama, L.; Arriortua, M. I.; Rojo, T. *J. Solid State Chem.* **2009**, *182*, 932−941. (e) Bazán, B.; Mesa, J. L.; Pizarro, J. L.; Rodríguez-Fernández, J.; Sanchez-Marcos, J.; Roig, A.; Molins, E.; Arriortua, M. I.; Rojo, T. *Chem. Mater.* **2004**, *16*, 5249−5259.

(6) (a) Fernández de Luis, R.; Urtiaga, M. K.; Mesa, J. L.; Larrea, E. S.; Iglesias, M.; Rojo, T.; Arriortua, M. I. *Inorg. Chem.* **2013**, *52*, 2615−2626. (b) Fernández de Luis, R.; Mesa, J. L.; Urtiaga, M. K.; Rojo, T.; Arriortua, M. I. *Eur. J. Inorg. Chem.* **2009**, *32*, 4786. (c) Larrea, E. S.; Mesa, J. L.; Pizarro, J. L.; Arriortua, M. I.; Rojo, T. *J. Solid State Chem.* **2007**, *180*, 1149.

(7) (a) Schindler, M.; Hawthorne, F. C.; Baur, W. H. *Can. Mineral.* **2000**, *38*, 1443−1456. (b) Livaje. *J. Coord. Chem.* **1998**, *178*−*180*, 999−1018. (c) Larrea, E. S.; Mesa, J. L.; Pizarro, J. L.; Rodríguez Fernández, J.; Arriortua, M. I.; Rojo, T. *Eur. J. Inorg. Chem.* **2009**, 3607−3612.

(8) (a) Larrea, E. S. Nuevos Vanadatos Híbridos de Metales de Transición. Síntesis Hidrotermal, Estudio Estructural y de sus Propiedades Espectroscópicas y Magnéticas. Doctoral thesis, Universidad del País Vasco (UPV/EHU), 2009. (b) Fernández de Luis, R.; Urtiaga, M. K.; Mesa, J. L.; Aguayo, A. T.; Rojo, T.; Arriortua, M. I. *CrystEngComm* **2010**, *12*, 1880−1886. (c) Fernández de Luis, R. Auto-Ensamblaje de Vanadatos Heterometálicos Basados en Redes Metal Orgánicas con Ligandos Bipodales. Doctoral Thesis, Universidad del País Vasco (UPV/EHU), 2009. (d) Calderón, A. Transformaciones Estructurales en Arquitecturas Supramoleculares Basadas en el Ligando PDC. Doctoral thesis, Universidad del País Vasco (UPV/EHU), 2012.

(9) Fernández de Luis, R.; Mesa, J. L.; Urtiaga, M. K.; Rojo, T.; Arriortua, M. I. *Eur. J. Inorg. Chem.* **2009**, 4786−4794.

(10) Fernández de Luis, R.; Urtiaga, M. K.; Mesa, J. L.; Vidal, K.; Lezama, L.; Rojo, T.; Arriortua, M. I. *Chem. Mater.* **2010**, *22*, 5543−5553.

(11) Fernández de Luis, R.; Mesa, J. L.; Urtiaga, M. K.; Larrea, E. S.; Rojo, T.; Arriortua, M. I. *Inorg. Chem.* **2012**, *51*, 2130−2139.

(12) Chen, C.-L.; Goforth, A. M.; Smith, M. D.; Su, C.-Y.; zur Loye, H.-C. *Angew. Chem., Int. Ed.* **2005**, *44*, 6673−6677.

(13) (a) Horike, S.; Dincă; Tamaki, K.; Long, J. R. *J. Am. Chem. Soc.* **2008**, *130*, 5854−5855. (b) Hong, D.-Y.; Hwang, Y. K.; Serre, C.; Férey, G.; Chang, J.-S. *Adv. Funct. Mater.* **2009**, *19*, 1537−1552. (c) Hasegawa, S.; Horike, S.; Matsuda, R.; Furukawa, S.; Mochizuki, K.; Kinoshita, Y.; Kitagawa, S. *J. Am. Chem. Soc.* **2007**, *129*, 2607−2614. (d) Platero-Prats, A.; de la Peña-ÓShea, V.; Iglesias, M.; Snejko, N.; Monge, A.; Gutíerrez-Puebla, E. *Chem. Cat. Chem.* **2010**, *2*, 147−149.

(14) Yingua, W. *J. Appl. Crystallogr.* **1987**, *20*, 258−259.

(15) Altomare, A.; Cascarano, G.; Giacovazzo, C.; Guagliardi, A. *J. Appl. Crystallogr.* **1993**, *26*, 343−350.

(16) Sheldrick, G. M. *SHELX97, Programs for Crystal Structure Analysis*; Institüt für Anorganische Chemie der Universität: Göttingen, Germany, 1998.

(17) Petříček, V, Dušek, M; Palatinus, L *JANA2006-Crystallographic Computing System*; Institute of Physics, Academy of Sciences of the Czech Republic: Prague, 2006.

(18) (a) Larrea, E. S.; Fernández de Luis, R.; Mesa, J. L.; Pizarro, J. L.; Urtiaga, M. K.; Rojo, T., Arriortua, M. I. In *Coordination Polymers and Metal Organic Frameworks: Properties, Types and Applications*; Ortiz, O. L.; Ramírez, L. D., Eds.; Nova Science Publisher Inc.: New York, 2012; Chapter 1, pp 1−58. (b) Schindler, M.; Hawthorne, F. C.; Baur, W. H. *Chem. Mater.* **2000**, *12*, 1248−1259. (c) Zavalij, P. Y.; Whittingham, M. S. *Acta Crystallogr.* **1999**, *B55*, 627−663.

(19) Brown, I. D. In *Structure and Bonding in Crystals*; O'Keeffe, M.; Navrotsky, A., Eds.;Academic Press: New York, 1981; Vol. *2*, p 1.

(20) (a) Frey, F. *Z. Kristallogr.* **1997**, *212*, 257−282. (b) Boysen, H.; Frey, F.; Schrader, H.; Eckold, G. *Phys. Chem. Minerals* **1991**, *17*, 629−635.

(21) (a) Blatov, A. V. *IUCr CompComm. Newslett.* **2006**, *7*, 4−7, http://www.topos.ssu.samara.ru. (b) Carluci, L.; Ciani, G.; Proserpio, D. M. *Coord. Chem. Rev.* **2003**, *246*, 247−289. (c) Ke, X.-J.; Li, D.-S.; Du, M. *Inorg. Chem. Commun.* **2011**, *14*, 788−803.

(22) He, Y.-C.; Hang, J.; Yang, G.-C.; Kan, W.-Q.; Ma, J.-F. *Chem. Commun.* **2012**, *48*, 7859−7861.

(23) Cao, G.-J.; Zheng, S.-T.; Fang, W.-H.; Yang, G.-Y. *Inorg. Chem. Commun.* **2010**, *13*, 834−836.

(24) (a) Colodrero, R. M. P.; Cabeza, A.; Olivera-Pastor, P.; Choquesillo-Lazarte, D.; Garcia-Ruiz, J. M.; Turner, A.; Ilia, G.; Maranescu, B.; Papathanasiou, K. E.; Hix, G. B.; Demadis, K. D.; Aranda, M. A. G. *Inorg. Chem.* **2011**, *50*, 11202−11211. (b) Choudhury, A.; Neeraj, S.; Natarajan, S.; Rao, C. N. R. *Angew. Chem. ,Int. Ed.* **2000**, *39*, 3091−3093. (c) Funahashi, Y.; Yoneda, A.; Taki, C.; Kosuge, M.; Ozawa, T.; Jitsukawa, K.; Masuda, H. *Chem. Lett.* **2005**, *34*, 1332−1334.

(25) (a) Frost, R. L.; Erickson, K. L.; Weier, M. L.; Carmody, O. *Spectrochim. Acta* **2005**, *A61*, 829−834. (b) Watanabe, H.; Okamoto, Y.; Furuya, K.; Sakamoto, A.; Tasumi, M. *J. Phys. Chem. A* **2002**, *106*, 3318−3324. (c) Furuya, K.; Kawato, K.; Yokoyama, H.; Sakamoto, A.; Tasumi, H. *J. Phys. Chem. A* **2003**, *107*, 8251−8258. (d) Zhuang, Z.; Cheng, J.; Jia, H.; Zeng, J.; Han, X.; Zhao, B.; Zhang, H.; Zhang, G.; Zhao, W. *Vibr. Spectr.* **2007**, *14*, 306−312. (e) Zubkov, V. G.; Surat, L. L.; Tyutyunnik, A. P.; Berger, I. F.; Tarakina, N. V.; Slobodin, B. V.; Kuznetsov, M. V.; Denisova, T. A.; Zhuravlev, N. A.; Perelyaeva, L. A.; Baklanova, I. V.; Shein, I. R.; Ivanovskii, A. L. *Phys. Rev.* **2008**, *B77*, 174113-1−174113-14. (f) Frost, R. L.; Erickson, K. L.; Weier, M. L.

Spectrochim. Acta A **2004**, *60*, 2419−2423. (g) Frost, R. L.; Kristy, L.; Weier, M. L.; Cardomy, O. *Spectrochim. Acta A* **2005**, 829−834.